Energy & Environmental Science

PAPER

View Article Online
View Journal | View Issue

Published on 03 February 2015. Downloaded by Harvard University on 09/04/2015 22:44:36.

Cite this: *Energy Environ. Sci.*, 2015, **8**, 1329

N-doped graphene quantum sheets on silicon nanowire photocathodes for hydrogen production†

Uk Sim,‡[a] Joonhee Moon,‡[b] Junghyun An,[a] Jin Hyoun Kang,[b] Sung Eun Jerng,[a] Junsang Moon,[a] Sung-Pyo Cho,[bc] Byung Hee Hong*[bd] and Ki Tae Nam*[a]

Received 14th November 2014
Accepted 3rd February 2015

DOI: 10.1039/c4ee03607g

www.rsc.org/ees

Photoelectrochemical hydrogen production from solar energy has been attracting much attention in the field of renewable energy technology. The realization of cost-effective hydrogen production by water splitting requires electrolysis or photoelectrochemical cells decorated with highly efficient co-catalysts. A critical requirement for catalysts in photoelectrochemical cells is not only the ability to boost the kinetics of a chemical reaction but also to exhibit durability against electrochemical and photoinduced degradation. In the race to replace previous noble-metal catalysts, the design of carbon-based catalysts represents an important research direction in the search for non-precious, environmentally benign, and corrosion-resistant catalysts. Herein, we suggest graphene quantum sheets as a catalyst for the solar-driven hydrogen evolution reaction on Si nanowire photocathodes. The optimum nanostructures of the Si photocathodes exhibit an enhanced photocurrent and a lower overpotential compared to those of a planar Si surface. This significant enhancement demonstrates how graphene quantum sheet catalysts can be used to produce Si nanowire photocathodes as hydrogen evolution reaction catalysts with high activity.

Broader context

Hydrogen production by solar energy has been widely studied as an environmentally friendly and sustainable energy source. Silicon-based electrodes can serve as photocathodes for hydrogen production under visible light because of their appropriate band structures. However, kinetic issues regarding the exchange current require an overpotential and the use of catalysts in the system. The development of catalysts for hydrogen production is of fundamental and technological importance. To solve the problems associated with previously reported noble metal-based catalysts, carbon-based catalysts serve as an important research direction in the search for low-cost, environmentally friendly, and corrosion-resistant catalysts. In this work, we fabricated graphene quantum sheets as a catalyst on Si nanowire photocathodes for the solar-driven hydrogen evolution reaction. Our approach in this study exploits a strategy for developing metal-free carbon-based catalysts with high efficiency for solar-driven hydrogen fuel production.

Introduction

The development of sustainable energy sources is an urgent issue because of the current level of energy consumption.[1] Renewable and sustainable energy sources must be developed because the present energy sources have several disadvantages such as CO_2 emission and limited deposits of fossil fuels.[2] Photoelectrochemical hydrogen production using solar energy represents an important and environmentally friendly technology with no carbon emissions.[3] The development of efficient and cheap photoelectrodes for water splitting is one of the fundamental challenges in hydrogen production.[4] Despite the intriguing advances in controlling the nanostructural interface and newly discovered material compositions for photoelectrodes, sluggish kinetic issues associated with a high overpotential remain some of the most difficult issues that need to be resolved.[5,6] Intense research into efficient, durable, and inexpensive hydrogen evolution reaction (HER) catalysts has been undertaken to solve the kinetic problem.[7–10] In general, precious metals such as platinum exhibit superior performance as HER catalysts; however, the unavoidable disadvantage of precious metals is their high cost.[11] A critical requirement for producing outstanding catalysts in a photoelectrochemical cell is not only the ability to boost the kinetics of the electrochemical reaction but also the ability to resist electrochemical

[a]*Department of Materials Science & Engineering, Seoul National University, 1 Gwanak-ro, Gwanak-gu, Seoul, 151-744, Korea. E-mail: nkitae@snu.ac.kr; Tel: +82-2-880-8305*

[b]*Department of Chemistry, Seoul National University, 1 Gwanak-ro, Gwanak-gu, Seoul, 151-744, Korea. E-mail: byunghee@snu.ac.kr; Tel: +82-2-882-6569*

[c]*National Center for Inter-University Research Facilities, Seoul National University, 1 Gwanak-ro, Gwanak-gu, Seoul, 151-744, Korea*

[d]*Graduate School of Convergence Science and Technology, Seoul National University, Suwon 443-270, Korea*

† Electronic supplementary information (ESI) available: Additional information, figures and table. See DOI: 10.1039/c4ee03607g

‡ These authors contributed equally to this work.

Published on 03 February 2015. Downloaded by Harvard University on 09/04/2015 22:44:36.

and photoinduced degradation. Herein we demonstrate that the combination of controlling a nanostructure of the photoelectrode and using a carbon-based hydrogen evolution catalyst represents a significant step toward enhancing the applied bias photon-to-current efficiency (ABPE). In the present work, a 430 mV decrease in overpotential was achieved using graphene quantum sheets on a silicon nanowire, which exhibited an enhanced effect comparable to that of platinum catalysts. Furthermore, the current density at the reversible potential *vs.* a reversible hydrogen electrode (RHE) exhibited a 101-fold enhancement relative to the current density achieved with planar silicon substrates.

The thermodynamic potential of water splitting is 1.23 V, which is observed by subtracting the reduction reaction and oxidation reaction in the photoelectrochemical reaction of water. At the anode, the oxidation reaction in the electrolysis of water is:

$$O_2 + 4e^- + 4H^+ \leftrightarrow 2H_2O, \quad E_{anodic} = 1.23\ V – 0.059(pH)\ V\ (vs.\ NHE) \quad (1)$$

whereas the reduction reaction at the cathode is:

$$4e^- + 4H^+ \leftrightarrow 2H_2,\ E_{cathodic} = 0\ V – 0.059(pH)\ V\ (vs.\ NHE) \quad (2)$$

where NHE is the normal hydrogen electrode and the standard potential is dependent on pH ($E_{half} = E - 0.059(pH)$ *vs.* NHE). Kinetically, however, when a voltage of 1.23 V is applied, electrolysis is difficult to induce, which results in no current flow. In this situation, a higher potential, which is referred to as the overpotential, η, is needed to drive the reaction at a certain rate. Moreover, if a current i_c flows at the cathode, a current i_a of the same magnitude must flow at the anode to complete the circuit, which requires the overpotential at both electrodes. The overpotentials at the cathode and anode are denoted as η_c and η_a, respectively. Therefore, the total applied potential, E_{appl}, is

$$E_{appl} = 1.23\ V + \eta_c + \eta_a \quad (3)$$

A higher overpotential requires a higher total applied voltage. Using an electrocatalyst for water splitting can reduce the overpotential required for the electrolysis of water.

In an effort to reduce the overpotential for the water splitting reaction, various catalysts have been deposited onto photoelectrode materials. Previously reported HER catalysts include pure metals, metal composites/alloys, compounds such as nonmetallic elements and molecular catalysts.[4,5,12–16] Among metal-based catalysts, Pt, Pd, and Ru are near the top of the volcano plot, exhibiting high catalytic activity toward the HER.[7] For example, Pt nanoparticles on p-type Si nanowires in aqueous electrolyte solutions can enhance the onset potential by approximately 0.42 V.[17] In view of economic issues, recent progress has been concentrated on the incorporation of metal nanoparticles into earth-abundant elements rather than on the use of noble metals alone.[11] Nonprecious metal catalysts and catalysts that are abundant in nature have also exhibited high activity toward the HER. Binary structures such as MoS_2, Mo_2N, Mo_2C, and Ni_2P and bimetallic compounds such as Co–Mo–N and Ni–Mo have been suggested as catalysts with high HER activity.[12,18–21] However, the rigorous and precise tuning of the composition of $A_xB_yM_z$ compounds, controlling the active sites in catalysts for the HER, and nanostructuring make optimization of the properties of catalysts for the HER difficult. Moreover, when deposited with catalysts, the saturation current density and the current density at a reversible potential *vs.* RHE significantly decrease because of light scattering by catalysts on the surface of the photoelectrodes.

To solve the problems associated with previously developed catalysts, carbon-based catalysts may represent an important research direction in the search for low-cost, environmentally friendly, and corrosion-resistant catalysts. Among carbon-based catalysts, graphene, in particular, possesses excellent transmittance and superior intrinsic carrier mobility; thus, several attempts have been made to use graphene as a catalyst.[22] Co-activated N and P heteroatoms adjacent to C atoms in the graphene matrix can affect such catalysts' valence orbital energy levels and thereby enhance their reactivity toward the HER.[23] Graphitic-carbon nitride combined with nitrogen-doped graphene also exhibits enhanced HER activity, with HER properties similar to those of well-established metallic catalysts.[24] Reduced graphene oxide containing catalytic active materials has exhibited improved activity in oxygen reduction reactions and oxygen evolution reactions as well as in the HER.[25–28] However, in most cases, the role of carbon materials is limited to an electrically conducting substrate or a support that increases the HER activity of other decorated active catalysts. Recently, we suggested that monolayer graphene deposited onto a planar Si electrode acts as an efficient HER electrocatalyst and that N_2 plasma treatment enhances its catalytic activity.[29] In this study, we further investigated N_2-plasma-treated graphene quantum sheets deposited on Si nanowire photocathodes as efficient HER electrocatalyst.

Controlling the surface structure of Si represents another important approach to improving photoelectrochemical performance. Si, one of the most abundant elements in the Earth's crust, can be used both as a photocathode and a photoanode for photochemical water splitting because its bandgap (1.12 eV) allows for the absorption of a significant portion of the solar spectrum.[30,31] However, the small band bending between the conduction band edge and the H^+/H_2 redox level of aqueous electrolytes limits the photoelectrochemical performance of Si relative to that of Si/non-aqueous solvent systems.[5] The application of an external potential or the use of catalysts is necessary for efficient operation under solar irradiation. To overcome this problem, a porous structure or a nanostructure can increase the current density of Si photoelectrodes by increasing the number of effective reaction sites between the Si semiconductor and the liquid electrolyte junction as well as by reducing the reflection of incident light.[6,32] A nanowire structure can increase the efficiency due to the orthogonalization of the direction of incident light absorption and charge carrier collection.[33] Therefore, the combination of an optimized Si nanowire photocathode and a graphene quantum sheet catalyst can boost the catalytic activity toward the photoelectrochemical HER.

 This journal is © The Royal Society of Chemistry 2015

Published on 03 February 2015. Downloaded by Harvard University on 09/04/2015 22:44:36.

Results and discussion

Measurements of photoelectrochemical performance show that N-doped graphene quantum sheets (N-GQSs) on a Si photoelectrode exhibit catalytic HER activity. Fig. 1 shows a schematic of hydrogen production on N-GQSs on Si nanowire arrays (SiNWs) in an acid solution under irradiation. Photons absorbed by the SiNWs generate minority carriers (electrons), which drift to the semiconductor/electrolyte interface where $2H^+$ is reduced to H_2; the N-GQSs serve as electrocatalysts for hydrogen production. In the schematic of the N-GQSs, gray, green, blue, and red spheres represent carbon, pyrrolic nitrogen, quaternary nitrogen, and pyridinic nitrogen atoms, respectively, based on high resolution X-ray photoelectron spectrum (XPS) measurements. The transmission electron microscopy (TEM) image and a size-distribution histogram indicate that the average diameter of the N-GQSs is 5 nm (Fig. S1†). N-GQSs were transferred to p-type silicon nanowires *via* drop-casting. The N-GQSs were converted from monolayer graphene on Cu foil using nitrogen plasma. After exposure to nitrogen plasma, the nano-sized GQSs were distributed on the Cu foil and were subsequently characterized by atomic force microscopy (AFM); the strong D peak of the sheets, which is related to the structural defects at the edges of graphene, was identified in the Raman spectrum. In addition, the doping of the GQSs with ~2.9% nitrogen was determined by the N 1s XPS spectrum, and the UV-vis absorption spectrum of the N-GQSs revealed an absorption band with a peak at 275 nm, as shown in Fig. S1.† The well-aligned SiNW arrays serve as an anti-reflector that enhances light absorption in the structure and increases the overall surface area; the N-GQSs act as electrocatalysts for hydrogen evolution.

The top-view and cross-sectional scanning electron microscopy (SEM) images of the N-GQSs on SiNWs are shown in Fig. 2a and b. The SiNWs exhibited an average diameter of ~400 nm, and lengths of up to ~5 μm. To determine the crystallinity, orientation, and morphology of the N-GQSs on SiNWs, TEM analyses were performed. The selected area electron diffraction pattern, with an incident beam axis of $[\bar{1}10]$ (Fig. S3†), indicated

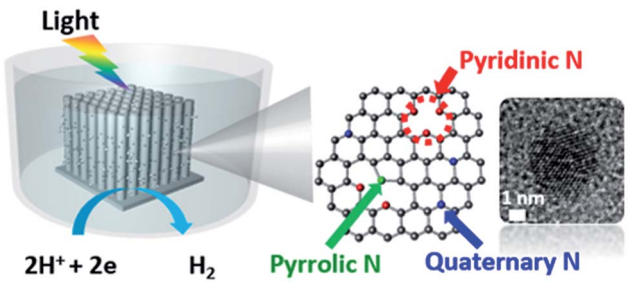

Fig. 1 Schematic of N-doped graphene quantum sheets (N-GQSs) decorated on a Si nanowire (SiNW) photocathode electrode. Photons absorbed by the SiNWs generate minority carriers (electrons), which drift to the semiconductor/electrolyte interface, where $2H^+$ is reduced to H_2; the N-GQSs serve as electrocatalysts for hydrogen production. The gray, green, blue, and red spheres in the schematic of N-GQSs represent the carbon, pyrrolic nitrogen, quaternary nitrogen, and pyridinic nitrogen atoms, respectively. The average diameter of the N-GQSs is 5 nm, as determined from a TEM image.

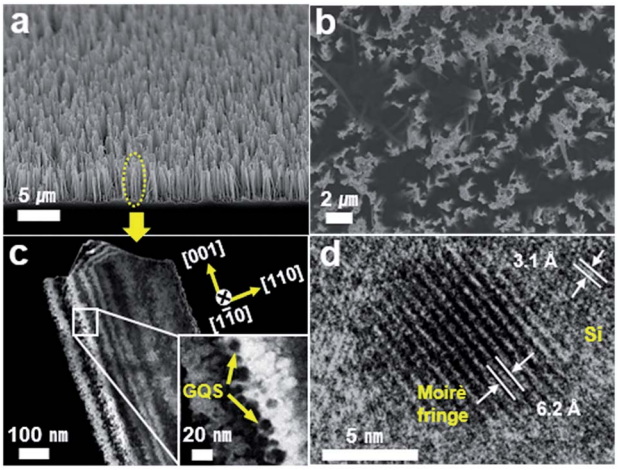

Fig. 2 SEM images of SiNW arrays on a p-silicon substrate obtained by a metal assisted chemical etching method. (a) Cross-section and (b) top-view. (c) Dark-field TEM images of N-GQSs on p-SiNWs. (d) High-resolution TEM image shows the Moiré pattern created by N-GQS in silicon lattices.

that a single-crystalline SiNW was well aligned along the [001] direction; the thickness fringes, brightness and dark line pattern indicate that the SiNW was etched as a column with angled edges, as shown in Fig. 2c. Moreover, the N-GQSs, which measured approximately 7 nm in diameter, were uniformly placed on the SiNWs, as indicated by dark-field TEM imaging (Fig. 2c); moreover, the formation of the N-GQSs was verified by high-resolution TEM (HRTEM). The HRTEM image shows the Moiré pattern created by the superposition of the mismatched crystalline lattices of the N-GQSs and SiNWs, as shown in Fig. 2d. The lattice plane spacing of p-Si was observed to be 3.1 Å, which corresponds to the silicon (100) plane (JCPDS, no. 24-1402). The Moiré pattern (6.2 Å) indicates mixed translational and rotational geometry. The corresponding spacing of the fringes was calculated as follows:[34]

$$a_m = \left(a_{GQS} \times a_{Si}\right) \Big/ \sqrt{a_{GQS2} + a_{Si2} - 2a_{GQS}a_{Si}\cos\left(\alpha_{GQS} - \alpha_{Si}\right)} \quad (4)$$

where a_m is the d-spacing of the Moiré pattern, a_{GQS} is the d-spacing of the N-GQS, and a_{si} is the d-spacing of Si. On the basis of eqn (4), the placement of an N-GQS on a SiNW with a 20 degree tilt was verified by the relationship between the Moiré fringe spacing and the Si lattice plane.

To investigate the dependence of a Si photoelectrode on its nanostructure, Si substrates of various nanostructures were fabricated by silver metal-assisted chemical etching.[35] Normal boron-doped p-type (100) Si substrates were immersed in an aqueous solution of 0.015 M silver nitrate and 5 M hydrofluoric acid. Continuous Si oxidation by the galvanic reduction of Ag^+ ions and the ensuing dissolution of silicon oxide by HF resulted in the [100] directional etching of the Si substrates. The etching time was varied between 20 min, 30 min, 120 min, and 180 min. Depending on the etching time, different Si nanostructures were observed as characterized by SEM (Fig. S5†). When the

Published on 03 February 2015. Downloaded by Harvard University on 09/04/2015 22:44:36.

etching time was shorter than 120 min, a porous nanostructure was observed. The transition of the surface structure from a porous to a nanowire structure occurred when the Si substrates were etched for 120 min. After this stage, the length of the nanowires was observed to increase with increasing etching time. Representative images of the SiNWs are shown in Fig. 2a and b.

For the evaluation of the photocathodic behavior of the nanostructured Si electrodes, the current density was measured as the potential was swept from 0.4 V to −1.0 V *vs.* RHE in a three-electrode cell. A 300 W Xe lamp was used to illuminate the Si photoelectrode with a light intensity of 100 mW cm^{-2} through an Air Mass 1.5 Global filter in an aqueous 1 M perchloric ($HClO_4$) acid solution (pH 0). Because the applied potential of the Si working electrode was negative (cathodic), the magnitude of the current density increased and saturated at a specific value of the applied potential. The current density at the saturation point is called the limiting current density or the saturation current density. As shown in Fig. 3a and Fig. S4,† the current density of the planar Si continued to increase until the length of the nanowires reached 5 μm as the surface became increasingly nanostructured. The limiting current density of bare planar Si was approximately −33 mA cm^{-2}. The surface area of the nanostructured Si substrate was greater than that of the planar structure. The reflectance of incident light could be reduced by the nanostructured Si surface. Although the surface of planar Si reflects approximately one quarter of the incident light, photon absorption is enhanced at the nanostructured surface because of its low reflectance. Nanostructured silicon wires have been reported to exhibit a light trapping effect,[36] which can enhance the current level for hydrogen production when the length of the Si nanowires is optimized to exhibit strong broadband optical absorption.[37] The nanowire structure also has the advantage of inducing the orthogonalization of light absorption and charge-carrier collection.[33] Thus, the minority carriers generated by incident solar light can move to the lateral side of each nanowire and participate in the hydrogen evolution reaction more quickly than in the planar structure. To calculate the photovoltage of the Si photoelectrode, the dark current density was also measured. The photovoltage is defined as the difference between the onset potentials under the dark and illuminated conditions. Fig. 2b shows the dark current densities of representative Si electrodes. The dark current density of the nanostructured electrodes was also greater than that of the planar Si substrate. The nanostructured photoelectrode (0.59 V of photovoltage) exhibited a positive shift in the photovoltage of 0.13 V relative to that of the planar Si electrode (0.46 V of photovoltage) as shown in Table S1.†

In measurements of the photoelectro-catalytic performance, N-GQSs on SiNWs exhibited catalytic activity toward the HER. As shown in Fig. 3a, the current density of the N-GQSs/planar Si structure increased gradually from 0 V *vs.* RHE and was saturated at approximately −35 mA cm^{-2} below −0.8 V *vs.* RHE at negative applied potentials. This current density is higher than that of planar Si without N-GQSs. Interestingly, measurements

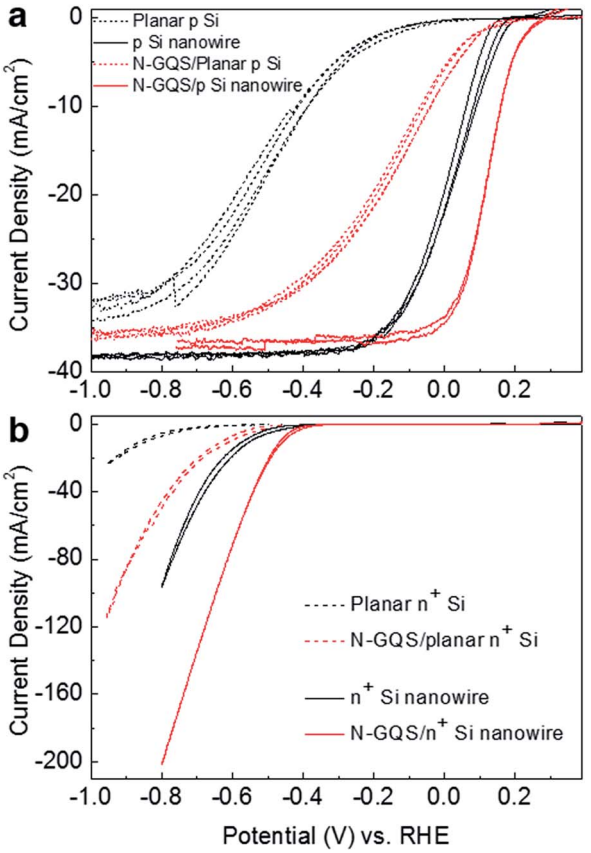

Fig. 3 Cyclic voltammograms of N-doped graphene quantum sheets (N-GQSs) on silicon photocathodes. (a) Photocurrent density–potential (*J*–*E*) curves for a lightly boron-doped planar p-Si electrode and Si nanowire deposited with N-GQSs. The Si nanowire was fabricated using a metal-catalyzed electroless method. (b) Polarization curves of N-GQS on heavily arsenic-doped n^+-type Si electrodes under dark conditions.

of the N-GQSs/planar Si structure showed that the overall current density–potential (*J*–*E*) curve was shifted by approximately 0.2 V toward positive potentials compared to that of planar Si without N-GQSs. The onset potential is defined as the potential at a photocurrent density of −1 mA cm^{-2}. The onset potential of N-GQSs/planar Si was 0.13 V *vs.* RHE, representing a positive shift of 0.30 V compared to the onset potential of bare Si (−0.17 V *vs.* RHE). Fig. 3b also shows the dark current densities of the heavily arsenic-doped n^+-type Si electrodes. Under the dark conditions, the positive shift in the onset potential of 0.21 V (−0.44 V *vs.* RHE for N-GQSs/planar Si) is also found to be higher than that of planar Si (−0.63 V *vs.* RHE for planar Si).

When incorporated into the nanostructured photoelectrode system, the N-GQSs exhibited much higher catalytic activity than that of the planar photoelectrode system. The onset potential of the N-GQSs/Si nanowire electrode was 0.26 V *vs.* RHE, which is 0.09 V higher than that of the Si nanowire without a catalyst (0.17 V *vs.* RHE). Both the increased onset potential and the current density at the reversible potential (0 V *vs.* RHE) showed an enhanced ABPE of 2.29%, which is greater

 This journal is © The Royal Society of Chemistry 2015

Published on 03 February 2015. Downloaded by Harvard University on 09/04/2015 22:44:36.

than that of the bare Si nanowire system (0.91%). ABPE is the applied bias photon-to-current efficiency:[38]

$$\mathrm{ABPE} = [j_{\mathrm{ph}}\ (\mathrm{mA\ cm^{-2}}) \times (V_{\mathrm{redox}} - V_{\mathrm{b}})\ (\mathrm{V})/P_{\mathrm{in}}\ (\mathrm{mW\ cm^{-2}})]_{\mathrm{AM\ 1.5\ G}} \times 100\ (\%) \quad (5)$$

where, j_{ph} is the photocurrent density obtained under an applied bias V_{b}, V_{redox} is the redox potential for hydrogen production (0 V), V_{bias} is the externally applied bias potential that is often necessary to achieve reasonable photocurrents, and P_{light} is the intensity of the incident light under AM 1.5 G conditions (~100 mW $\mathrm{cm^{-2}}$). The enhanced photocatalytic performance indicates a synergistic effect between the N-GQSs and Si nanowire structures; moreover, the N-GQSs act as effective HER catalysts on the Si photocathode. Compared to previously reported carbon-based catalysts on the Si system, the N-GQSs/Si nanowire system exhibits a higher ABPE.

To investigate the electrocatalytic activity of the N-GQSs, we measured cyclic voltammetry using a rotating disk electrode (RDE) system. To fabricate the working electrode, an N-GQSs solution was transferred to a glassy carbon (GC) tip that was inert in an aqueous solution. As shown in Fig. 4a, in the *J–E* curves obtained by the RDE measurements, the current density associated with the water splitting reaction exponentially increased after the onset point as the potential was swept from 0.1 V to −0.45 V. For comparison with the potential for the HER in the RDE system, the potential required for attaining −5 mA $\mathrm{cm^{-2}}$ of HER current density was measured for graphene monolayer/GC, N-GQSs/GC, and Pt/GC systems. Also for comparison, the catalytic effect of graphene monolayer without plasma treatment was measured using RDE system. The potential required for attaining −5 mA $\mathrm{cm^{-2}}$ of HER current density was −0.32 V *vs.* RHE for the graphene monolayer without plasma treatment. The potential for the N-GQSs/GC electrode at −5 mA $\mathrm{cm^{-2}}$ was −0.22 V *vs.* RHE; this potential was positively (anodically) shifted by 100 mV relative to that for the monolayer graphene. This result indicates that the N-GQSs and monolayer graphene exhibit electrocatalytic activity toward the HER.

To gain further quantitative insight into the catalytic activity of the N-GQSs, the *J–E* curves in Fig. 4a were converted into plots of the potential as a function of the logarithm of *J*. This potential–log *J* plot is called a Tafel plot. The measured potentials were corrected for the iR losses that originated from the resistance of the interface between the electrode and the electrolyte. Analysis of the impedance spectra revealed that the resistances of the graphene monolayer and N-GQSs/GC were 7.5 and 8.0 Ω, respectively. The Tafel plot provides two parameters for estimating the electrocatalytic activity: the Tafel slope and the exchange current density. The Tafel slope is defined to be a measure of the potential increase required for increasing the resulting current by one order of magnitude. The graphene monolayer exhibited a Tafel slope of 75 mV per decade, and the N-GQSs/GC exhibited a slope of 45 mV per decade, 30 mV lower than that of the graphene monolayer. For comparison with a well-known catalyst, Pt particles were deposited onto GC and the electro-catalytic activity of the resulting electrode was

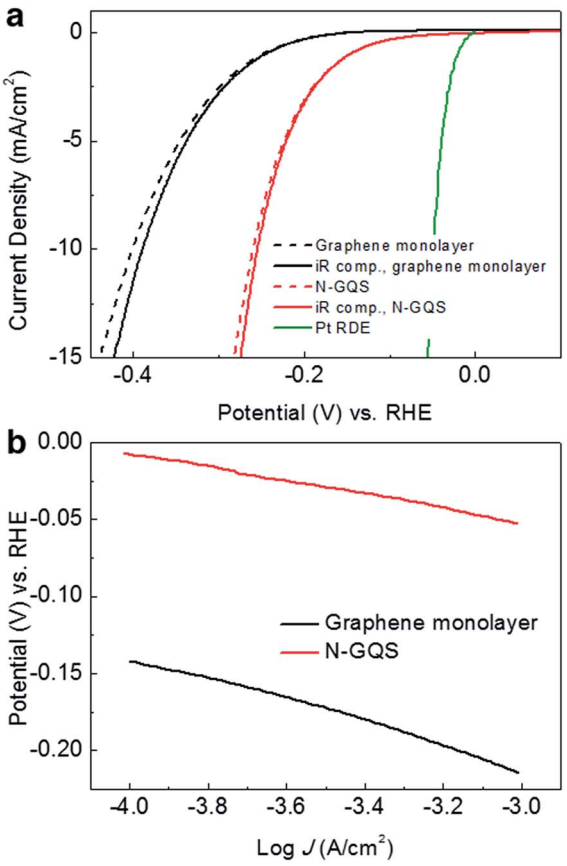

Fig. 4 Electrochemical activity of a graphene monolayer and N-GQSs on glassy carbon (GC) electrodes in a rotating disk electrode system. (a) Cyclic voltammograms (CV) of a graphene monolayer on GC, N-GQSs on GC, and Pt/C on GC. CV data obtained compensating for ohmic drop (iR) losses are also plotted (dashed curves). (b) Tafel plots derived from the CV data in (a).

measured. The applied potential required to obtain −5 mA $\mathrm{cm^{-2}}$ was −0.04 V *vs.* RHE, which represents a positive shift of 0.18 V relative to that of the N-GQSs/GC electrode. The Tafel slope of Pt-GC was 42 mV per decade, which is similar to that of the N-GQSs/GC. For previously reported carbon-based catalysts, the potential required to attain −5 mA $\mathrm{cm^{-2}}$ was −0.5 V *vs.* RHE for N-doped graphene and −0.3 V *vs.* RHE for graphitic C_3N_4, respectively.[23,24] The Tafel slope was reported to be 116 mV per decade for N-doped graphene and 51.5 mV per decade for graphitic C_3N_4 when deposited as a mixture with Nafion or carbon black on GC, respectively.

The Tafel slope provides an indication of which reaction steps are possible in the HER among the following:[39]

$$\mathrm{H_3O^+ + e^- \rightarrow H_{ads} + H_2O\ Volmer\ reaction} \quad (6)$$

$$\mathrm{H_{ads} + H_3O^+ + e^- \rightarrow H_2 + H_2O\ Heyrovsky\ reaction} \quad (7)$$

$$\mathrm{H_{ads} + H_{ads} \rightarrow H_2\ Tafel\ reaction} \quad (8)$$

where H_{ads} is adsorbed H, (6) is a discharge step, (7) is a desorption step, and (8) is a recombination step. Considering the adsorbed hydrogen coverage (θ_H) on the surface of an

Published on 03 February 2015. Downloaded by Harvard University on 09/04/2015 22:44:36.

electrode, if the recombination of adsorbed hydrogen (the Tafel reaction) is the rate-determining step for the HER and if the coverage is very high ($\theta_H \approx 1$), the measured Tafel slope will be 30 mV per decade. However, if the electrochemical desorption step (the Heyrovsky reaction) is the rate-determining step, a Tafel slope of 40–118 mV per decade is measured and is dependent on the value of θ_H (0–1).[40] The observed Tafel slope of 45 mV per decade in the present work indicates that the kinetics of the HER on the graphene monolayer/GC and N-GQS/GC electrodes is determined by the Heyrovsky reaction.

The exchange current density (J_0) of the N-GQS catalyst was also analyzed. During hydrogen evolution, the current I can be described by the following equation:[7]

$$I = -e(r^+ - r^-) \quad (9)$$

where $r^+ - r^-$ is the net rate of the electron transfer between the oxidation ($4e^- + 4H^+ \leftarrow 2H_2$) and the reduction ($4e^- + 4H^+ \rightarrow 2H_2$) from eqn (2). The exchange current is the sum of the forward and backward rates when eqn (2) is in equilibrium. The ability of a given material to catalyze the HER is usually measured by J_0, which is the rate of hydrogen evolution per surface area at the electrode potential when the reaction is at equilibrium. The J_0 is also defined as the current density at zero overpotential. The catalytic effect originates from the improvement of the rate of charge transfer at the interface between the electrode and the electrolyte or from a decrease in the activation energy barrier for a chemical reaction; these catalytic effects are represented by J_0. A high value of J_0 indicates that electron transfer or the adsorption/desorption of protons at the electrode/electrolyte can occur more easily, with a lower kinetic barrier. The value of J_0 can be obtained by extrapolating the Tafel plot in Fig. 4b and extracting the current density at 0 V *vs.* RHE. The N-GQS/GC electrode exhibited an enhanced J_0 of 7.1×10^{-5} A cm^{-2}, which was 26.3 times greater than the J_0 of monolayer graphene on GC (2.7×10^{-6} A cm^{-2}). The J_0 of the N-GQSs was also compared with that of other carbon-based catalysts (Table S3†). The reported carbon-based catalysts exhibited a lower J_0 than that of our N-GQS electrode. In addition, a metal-free carbon catalyst doped with nitrogen and phosphorus exhibited a J_0 of 2.4×10^{-7} A cm^{-2} and a graphitic C_3N_4 catalyst with nitrogen-doped graphene exhibited 3.5×10^{-6} A cm^{-2} of J_0.[23,24]

Fig. 5 summarizes the experimental data for the Si and GC electrodes. As shown in Fig. 5b, our N-GQS catalyst exhibited a lower Tafel slope and a higher J_0 compared to those of other reported carbon-based HER catalysts. Moreover, considering its role as a co-catalyst on the photoelectrode, the N-GQS/Si nanowire system exhibited better photoelectrochemical performance in terms of ABPE and onset potential than any other reported catalyst/photoelectrode system (Fig. 5a). Using only a non-metal carbon-based catalyst without incorporating a noble catalyst, the ABPE increased to 2.29% by the combination of the nanostructured photoelectrode and N-GQS catalyst. The good HER activity of the N-GQSs is attributed to abundant defects introduced by the plasma treatment. Moreover, high-resolution XPS results show that N-sites are classified into

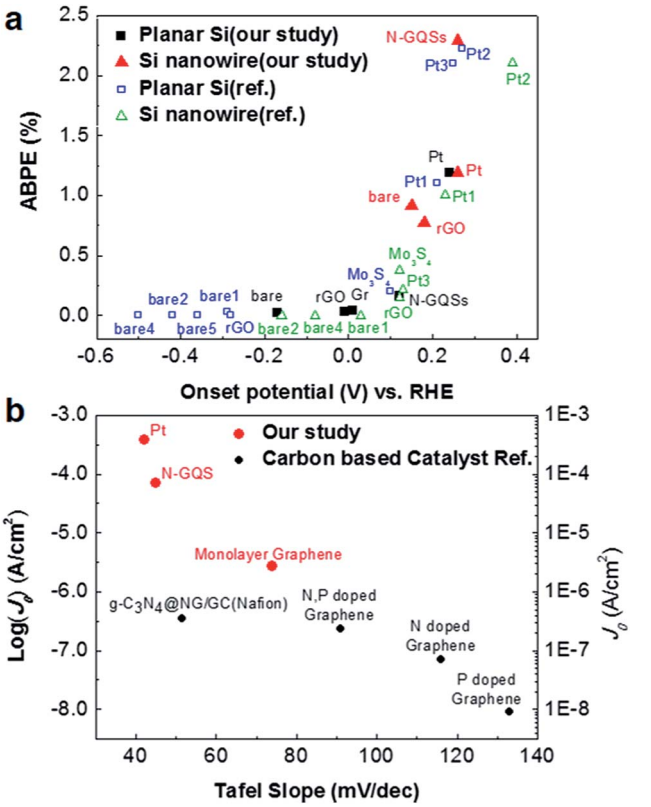

Fig. 5 Summary of the experimental data for Si and glassy carbon (GC) electrodes. (a) The photoelectrochemical performance of p-type Si-based photoelectrodes. 'Onset potential' and 'ABPE' indicate the potential at −1 mA cm^{-2} *vs.* RHE and the applied bias photon-to-current efficiency, respectively; 'bare' indicates the performance of the bare electrode without a deposited catalyst. (b) Electrochemical performance of N-GQSs on a GC electrode and other HER catalysts determined using a rotating disk electrode system. J_0 indicates the exchange current density. References can be found in the ESI (Tables S2 and S3†).

pyridinic (2.07 at%), pyrrolic (0.45 at%), and a small number of quaternary nitrogen atoms (0.16 at%), which act as the good catalytic sites for HER (Fig. S1e†). A previous report also suggested that N-doping on graphene could significantly improve the HER by providing additional active sites[23] and theoretical computation shows favorable N-sites for H adsorption.[41] We are investigating various N-sites with density functional theory for understanding the precise mechanism of HER.

To further study the electrochemical performance of the N-GQS/Si electrode, capacitance, impedance, and transient photoresponse measurements were performed, the results of which are shown in Fig. 6. Capacitance measurements of the N-GQS/Si nanowire and bare Si nanowire electrodes were performed as the potential was swept from 0.6 V to −0.5 V *vs.* RHE in a three-electrode cell without illumination. On the basis of the capacitance results, the flat band potential of the Si nanowire and N-GQS/Si nanowire electrodes were calculated using the Mott–Schottky relationship:[42]

$$1/C_{sc}{}^2 = 2(E - E_{fb} - kT/e)/(e\varepsilon\varepsilon_0 N) \quad (10)$$

This journal is © The Royal Society of Chemistry 2015

Published on 03 February 2015. Downloaded by Harvard University on 09/04/2015 22:44:36.

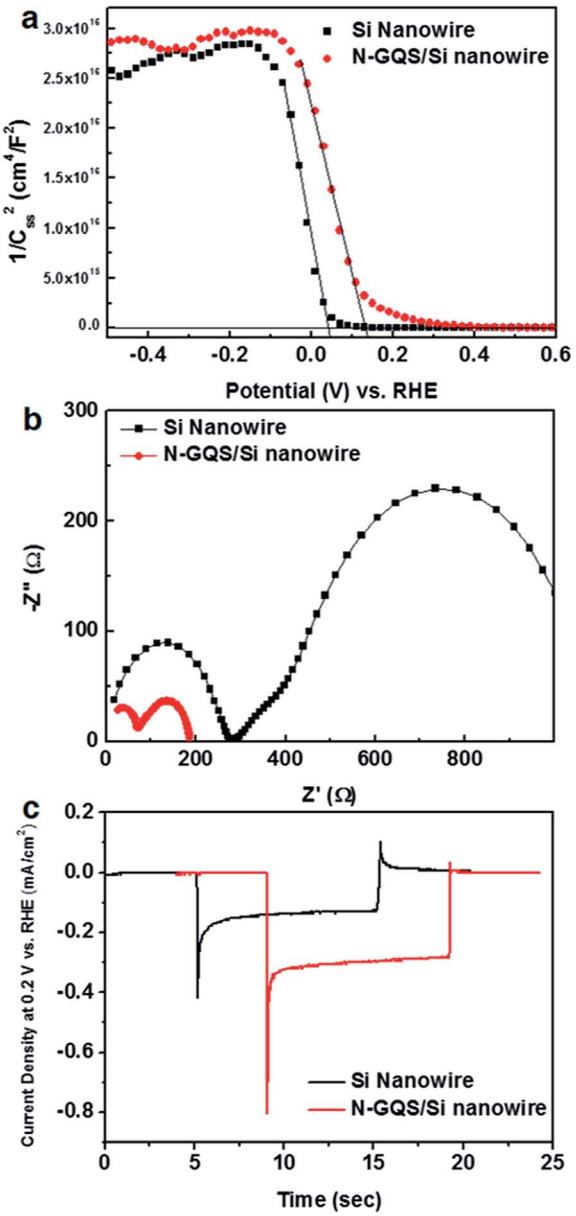

Fig. 6 Comparison of the electrochemical activity of Si nanowire and N-GQSs on a Si nanowire. (a) Mott–Schottky plots from capacitance measurement as a function of potential *vs.* RHE under dark conditions. (b) Nyquist plot for Si nanowire and N-GQSs on a Si nanowire at 0 V *vs.* RHE under illumination. (c) The transient curve of the photocurrent from Si nanowire and N-GQSs on a Si nanowire when the light was turned on and turned off at 0 V *vs.* RHE.

where C_{sc} is the capacitance of the space charge region, ε is the dielectric constant of the semiconductor, ε_0 is the permittivity of free space, N is the donor density (electron donor concentration for an n-type semiconductor or hole acceptor concentration for a p-type semiconductor), E is the applied potential, and E_{fb} is the flat band potential. Fig. 6a shows the typical Mott–Schottky plots for a p-type silicon semiconductor. The donor density was calculated from the slope, and E_{fb} was determined by extrapolation to a capacitance of zero. On the basis of these relations, the N-GQSs/Si nanowire electrode exhibited an E_{fb} of 0.13 V *vs.* RHE, whereas the E_{fb} of the bare Si nanowires was 0.02 V *vs.* RHE, as shown in Fig. 6a. According to the equation: $E_b = E - E_{fb}$, the applied potential determines the magnitude of band bending (E_b) in the semiconductor and E_{fb}.[43] As E_{fb} increases positively, the absolute value of E_b increases because the applied potential, E, is always negative under the cathodic reaction for proton reduction. Higher band bending at the interface between the electrode and electrolyte promotes faster charge separation of generated electrons and holes.[44] The possibility of charge recombination or surface trapping at sub-band gap energy levels may also be diminished. The higher E_{fb} of the N-GQS/SiNW electrode relative to that of the bare SiNW electrode appears to have augmented the extent of band bending in the depletion region of the semiconductor near the solid/solution interface because of the relationship between E_b and E_{fb}. Moreover, the doping density of bare SiNW and N-GQSs/SiNW is also calculated from the Mott–Schottky relationship. Using eqn (10), the bare SiNW shows a donor density of 4.46×10^{15} cm^{-3}, which corresponds to the resistivity of 10^0 to 10^1 ohm cm for boron doped p-Si.[45] The N-GQS/SiNW electrodes show a donor density of 5.74×10^{15} cm^{-3}. From the donor density results, N-GQSs deposited on a SiNW showed a slight increase of the donor density, which might change the electrochemical properties at the semiconductor/liquid interface. Zheng *et al.* reported that the N dopant adjacent to a C atom in a graphene matrix acts as an electron acceptor through the analysis of the natural bond orbital population.[23] Likewise, the N dopant on GQSs might also act as an active catalytic site for HER.

Impedance measurements were also performed to study the enhanced electrochemical properties of the N-GQS/SiNW system. Under an illumination intensity of 100 mW cm^{-2} with a frequency of 10^6 – 1 Hz and an amplitude of 5 mV in a three electrode system, electrochemical impedance spectroscopy was performed at 0 V *vs.* RHE. Fig. 6b shows a Nyquist plot representing a typical impedance result. In Fig. 6b, the N-GQS/SiNW electrode shows two semicircles that are smaller than those exhibited by the Si nanowire electrode. On the basis of the results gathered from these two semicircles, two capacitance elements can be assigned: the capacitance of the charge depletion layer in the semiconductor and the capacitance of the double layer at the semiconductor/electrolyte interface. In the high-frequency region, the charge transfer process in the depletion layer of the semiconductor dominates, whereas charge transfer across the double layer at the semiconductor/electrolyte interface is dominant in the low-frequency region.[46] In the case of the N-GQS/SiNW electrodes, the two semicircles indicating charge transfer processes in the double layers at the solid/solution interface and in the depletion region of the semiconductor are smaller than those of the bare SiNWs. The smaller semicircle in the low frequency range means that the charge transfer resistance of the N-GQSs/SiNW in the double layer is lower than that of the bare SiNW. The charge transfer resistance is also related to the kinetic barrier energy for the faradaic reactions across the double.[46] Thus, N-GQSs might promote the faradaic reactions by reducing the charge transfer resistance across the double layer. A similar charge transfer

Published on 03 February 2015. Downloaded by Harvard University on 09/04/2015 22:44:36.

mechanism in hydrogen production was also reported using a reduced graphene oxide catalyst.[28] From the result of the smaller semicircle in the high frequency range, the charge transfer resistance of the semiconductor depletion layer in the N-GQSs/SiNW is also lower than that of the bare SiNW. The charge transfer resistance in the semiconductor depletion layer is also correlated with the higher photocurrent response because of the higher band bending in the depletion layer.[44,47]

Transient photoresponse measurements were also performed to determine the factors enhancing the photoelectrochemical performance of the N-GQS/SiNW electrodes; the results are shown in Fig. 6c. The transient behavior of the N-GQS/SiNW and bare SiNW electrodes was measured at 0.2 V *vs.* RHE using a chopped illumination system. Fig. 6c shows the transient behavior of the N-GQS/Si and bare Si electrodes without a catalyst. The light was turned on and turned off after 10 s while the potential was maintained at 0.2 V *vs.* RHE. At the moment when the light was turned on, the current density reached a peak, which is referred to as the initial photocurrent density (J_{in}). The J_{in} values of the N-GQS/Si nanowire and bare Si nanowire electrodes were -0.80 mA cm^{-2} and -0.42 mA cm^{-2}, respectively. The current density then saturated, and the saturated photocurrent density (J_{st}) under illumination was -0.30 mA cm^{-2} for the N-GQS/Si nanowire electrode and -0.13 mA cm^{-2} for the bare Si nanowire electrode. At the moment when the light was turned off, the current density again showed an oscillating plot, and the current density at the peaks was designated as J_{off}. The J_{off} values of the N-GQS/Si nanowire and Si nanowire electrodes were -0.02 mA cm^{-2} and -0.12 mA cm^{-2}, respectively. The high $J_{st}/J_{in,\ N\text{-}GQSs}$ ratio of 0.375 and small J_{off} of the N-GQS/Si nanowire electrode suggest that fewer carriers were trapped and that less recombination occurred at the surface state of the electrode surface, in comparison with those of the surface state of the bare Si nanowire sample ($J_{st}/J_{in,\ bare} = 0.309$). Together, the capacitance and impedance results indicate that the N-GQS/Si nanowire electrode can contribute to charge separation by inducing favorable band bending and boosting the charge transfer rate, which enhance the electrode's HER performance. To summarize, the results obtained from the capacitance, impedance, and transient photoresponse measurements indicate that the N-GQS/SiNW electrode enhances the HER activity by reducing the possibility of charge recombination and lowering the kinetic barriers for the HER at the interface between the Si semiconductor and electrolyte solution.

Conclusions

We fabricated N-doped graphene quantum sheets (N-GQSs) as a catalyst for the solar-driven hydrogen evolution reaction on Si nanowire photocathodes. The onset potential for the Si nanowire photocurrent significantly shifted toward the anodic direction without a change in the saturation current density. N-GQSs exhibited excellent catalytic activity for the photoelectrochemical HER on Si nanowire photocathodes. The results showed that the N-GQS electrodes exhibited an ABPE of 2.29%, which is higher than that of any other carbon-based photoelectrochemical HER catalysts reported to date. Our approach in this study involved a strategy for developing metal-free carbon-based catalysts with high efficiency for solar-driven hydrogen fuel production.

Experimental

Synthesis of graphene quantum sheets

A copper foil (10×10 cm^2) was inserted into a quartz tube and then heated to 1000 °C for 40 min with flowing 5 sccm H_2. After reaching 1000 °C, the sample was annealed for 20 min under the same conditions. The gas mixture of 50 sccm CH_4 and 5 sccm H_2 was flowed for 30 min at a pressure of 8 Torr. After growth, the monolayer graphene on the back-side of copper was removed using oxygen plasma (100 W RF power, 12 s). Next, the N-GQSs were prepared by irradiating the graphene on the front-side of the copper foil with nitrogen plasma (10 W RF power, 12 s). Finally, the N-GQSs were floated on a 0.1 M ammonium persulfate etchant to remove the Cu substrate. After the Cu was removed, the floating N-GQSs were dispersed in a common organic solvent such as dichloromethane by solvent extraction.[48]

Preparation of Si nanowire (SiNW) photocathodes

Boron-doped (p-type) single-crystal Si wafers (4-inch diameter, 500 mm thickness, doped to achieve a resistivity of 10–15 Ω cm, oriented along the (100) plane) were purchased from Namkang Co. Ltd. $AgNO_3$ powder (99.5%) and HF (48–51 wt%) were purchased from Sigma Aldrich, and concentrated nitric acid solution (70 wt%) was purchased from Daejung Chemicals. The wafers were cut into 1 cm^2 pieces and successively cleaned in acetone, 2-propanol and deionized water for 10 min under sonication.

Each of the Si nanostructures was fabricated by the metal-catalyzed electroless etching method in a 20 mL aqueous solution of $AgNO_3$ (0.015 M) and HF (5 M) for etching times of 20 min, 30 min, 120 min, or 180 min (Fig. S5†). Excess Ag residues that could be contaminated during the electroless etching were removed by washing with 70% nitric acid solution for two hours.

A SiNW photocathode was fabricated by establishing an ohmic contact at the back side of a Si substrate. After the native oxide layer was removed from the Si surface using HF, a gallium–indium eutectic alloy was loaded onto the surface, followed by the application of silver conductive paste on a copper wire; the resulting assembly was then dried at 100 °C. To insulate and protect the back contact of the Si substrate, epoxy was applied over the entire sample except for the area that was illuminated on the front side. After the bare Si cell was fabricated, N-GQSs were transferred onto the Si surface *via* drop-casting.

Electrochemical measurements

Photoelectrochemical measurements were performed in a three-electrode cell using an electrochemical analyzer (CHI 760E, CH Instruments, Inc.). Schematic illustration and photographic images of hydrogen evolution reaction on a N-

 This journal is © The Royal Society of Chemistry 2015

Published on 03 February 2015. Downloaded by Harvard University on 09/04/2015 22:44:36.

GQS/Si photocathode are shown in Fig. S6.†Pt foil and Pt wire were used as the counter electrodes, and a Ag/AgCl/3 M NaCl electrode was used as the reference electrode. The reference electrode was carefully calibrated with respect to the RHE at 25 °C in an aqueous 1 M perchloric acid solution saturated with high purity H_2. The RHE was calibrated to between −0.201 V and −0.203 V *vs.* the Ag/AgCl reference electrode (Fig. S7†). To evaluate the photoelectrochemical behavior, visible light from a 300 W Xe lamp was illuminated onto the substrate with a light intensity of 100 mW cm^{-2} using a glass Air Mass 1.5 Global filter. For the electrochemical study, the Rotating Disk Electrode (RDE) system was purchased from PINE, Inc., and a glass carbon tip was used for the RDE measurements (dia. 5 mm). For comparison, 10 μL of Pt catalyst ink mixed with 5 wt% Nafion was loaded onto the GC and dried at 110 °C. RDE measurements were performed at a rotation speed of 1000 rpm and at a scan rate of 5 mV s^{-1}.

Characterization

Raman spectra were collected using a Renishaw micro-Raman spectrometer with an excitation wavelength of 514.5 nm emitted from an Ar laser. The spot diameter was ~2 μm, and a 50× objective lens was used. Oxygen plasma treatment (SNTEK) was carried out at a radio-frequency (rf) power of 100 W for 13 s under a pressure of 140 mTorr for the back side of graphene on Cu and the nitrogen plasma was accelerated at an rf power of 10 W over an exposure time of 12 s under a pressure of 120 mTorr on graphene.

Acknowledgements

This research was supported by the Basic Science Research Program (2011-0011225, 2011-0017587, 2012M3A7B4049807), the Global Frontier R&D Program of the Center for Multiscale Energy System (2011-0031574), the Global Research Lab (GRL) Program (2011-0021972), and the Fusion Research Program for Green Technologies through the National Research Foundation of Korea (2012M3C1A1048863), funded by the Ministry of Science, ICT & Future, Korea. This research was also supported by the Ministry of Science, ICT & Future, through the Research Institute of Advanced Materials (RIAM).

References

1 J. A. Turner, *Science*, 2004, **305**, 972–974.
2 N. S. Lewis and D. G. Nocera, *Proc. Natl. Acad. Sci. U. S. A.*, 2006, **103**, 15729–15735.
3 M. G. Walter, E. L. Warren, J. R. McKone, S. W. Boettcher, Q. Mi, E. A. Santori and N. S. Lewis, *Chem. Rev.*, 2010, **110**, 6446–6473.
4 T. R. Cook, D. K. Dogutan, S. Y. Reece, Y. Surendranath, T. S. Teets and D. G. Nocera, *Chem. Rev.*, 2010, **110**, 6474–6502.
5 S. W. Boettcher, E. L. Warren, M. C. Putnam, E. A. Santori, D. Turner-Evans, M. D. Kelzenberg, M. G. Walter, J. R. McKone, B. S. Brunschwig, H. A. Atwater and N. S. Lewis, *J. Am. Chem. Soc.*, 2011, **133**, 1216–1219.
6 U. Sim, H.-Y. Jeong, T.-Y. Yang and K. T. Nam, *J. Mater. Chem. A*, 2013, **1**, 5414–5422.
7 J. K. Nørskov, T. Bligaard, A. Logadottir, J. R. Kitchin, J. G. Chen, S. Pandelov and U. Stimming, *J. Electrochem. Soc.*, 2005, **152**, J23–J26.
8 T. F. Jaramillo, J. Bonde, J. Zhang, B.-L. Ooi, K. Andersson, J. Ulstrup and I. Chorkendorff, *J. Phys. Chem. C*, 2008, **112**, 17492–17498.
9 Y. Hou, A. B. Laursen, J. Zhang, G. Zhang, Y. Zhu, X. Wang, S. Dahl and I. Chorkendorff, *Angew. Chem., Int. Ed.*, 2013, **52**, 3621–3625.
10 Y. Yan, B. Xia, Z. Xu and X. Wang, *ACS Catal.*, 2014, **4**, 1693–1705.
11 C. Chen, Y. Kang, Z. Huo, Z. Zhu, W. Huang, H. L. Xin, J. D. Snyder, D. Li, J. A. Herron, M. Mavrikakis, M. Chi, K. L. More, Y. Li, N. M. Markovic, G. A. Somorjai, P. Yang and V. R. Stamenkovic, *Science*, 2014, **343**, 1339–1343.
12 J. R. McKone, E. L. Warren, M. J. Bierman, S. W. Boettcher, B. S. Brunschwig, N. S. Lewis and H. B. Gray, *Energy Environ. Sci.*, 2011, **4**, 3573–3583.
13 B. Marsen, B. Cole and E. L. Miller, *Sol. Energy Mater. Sol. Cells*, 2008, **92**, 1054–1058.
14 M. W. Kanan, Y. Surendranath and D. G. Nocera, *Chem. Soc. Rev.*, 2009, **38**, 109–114.
15 A. Kudo and Y. Miseki, *Chem. Soc. Rev.*, 2009, **38**, 253–278.
16 J. Ran, J. Zhang, J. Yu, M. Jaroniec and S. Z. Qiao, *Chem. Soc. Rev.*, 2014, **43**, 7787–7812.
17 I. Oh, J. Kye and S. Hwang, *Nano Lett.*, 2011, **12**, 298–302.
18 D. H. Youn, S. Han, J. Y. Kim, J. Y. Kim, H. Park, S. H. Choi and J. S. Lee, *ACS Nano*, 2014, **8**, 5164–5173.
19 R. K. Shervedani and A. Lasia, *J. Electrochem. Soc.*, 1998, **145**, 2219–2225.
20 B. Cao, G. M. Veith, J. C. Neuefeind, R. R. Adzic and P. G. Khalifah, *J. Am. Chem. Soc.*, 2013, **135**, 19186–19192.
21 S. Chen, J. Duan, Y. Tang, B. Jin and S. Zhang Qiao, *Nano Energy*, 2015, **11**, 11–18.
22 K. S. Novoselov, A. K. Geim, S. V. Morozov, D. Jiang, M. I. Katsnelson, I. V. Grigorieva, S. V. Dubonos and A. A. Firsov, *Nature*, 2005, **438**, 197–200.
23 Y. Zheng, Y. Jiao, L. H. Li, T. Xing, Y. Chen, M. Jaroniec and S. Z. Qiao, *ACS Nano*, 2014, **8**, 5290–5296.
24 Y. Zheng, Y. Jiao, Y. Zhu, L. H. Li, Y. Han, Y. Chen, A. Du, M. Jaroniec and S. Z. Qiao, *Nat. Commun.*, 2014, **5**, 3783–3791.
25 Y. Liang, Y. Li, H. Wang, J. Zhou, J. Wang, T. Regier and H. Dai, *Nat. Mater.*, 2011, **10**, 780–786.
26 J.-D. Qiu, G.-C. Wang, R.-P. Liang, X.-H. Xia and H.-W. Yu, *J. Phys. Chem. C*, 2011, **115**, 15639–15645.
27 Q. Xiang, J. Yu and M. Jaroniec, *Chem. Soc. Rev.*, 2012, **41**, 782–796.
28 Z. Huang, P. Zhong, C. Wang, X. Zhang and C. Zhang, *ACS Appl. Mater. Interfaces*, 2013, **5**, 1961–1966.
29 U. Sim, T.-Y. Yang, J. Moon, J. An, J. Hwang, J.-H. Seo, J. Lee, K. Y. Kim, J. Lee, S. Han, B. H. Hong and K. T. Nam, *Energy Environ. Sci.*, 2013, **6**, 3658–3664.

Published on 03 February 2015. Downloaded by Harvard University on 09/04/2015 22:44:36.

30 Y. Hou, B. L. Abrams, P. C. K. Vesborg, M. E. Björketun, K. Herbst, L. Bech, A. M. Setti, C. D. Damsgaard, T. Pedersen, O. Hansen, J. Rossmeisl, S. Dahl, J. K. Nørskov and I. Chorkendorff, *Nat. Mater.*, 2011, **10**, 434–438.
31 Y. W. Chen, J. D. Prange, S. Dühnen, Y. Park, M. Gunji, C. E. D. Chidsey and P. C. McIntyre, *Nat. Mater.*, 2011, **10**, 539–544.
32 J. Oh, T. G. Deutsch, H.-C. Yuan and H. M. Branz, *Energy Environ. Sci.*, 2011, **4**, 1690–1694.
33 B. M. Kayes, H. A. Atwater and N. S. Lewis, *J. Appl. Phys.*, 2005, **97**, 114302–114311.
34 D. B. Williams and C. B. Carter, *Transmission Electron Microscopy*, Springer, 2009.
35 K. Peng, H. Fang, J. Hu, Y. Wu, J. Zhu, Y. Yan and S. Lee, *Chem.–Eur. J.*, 2006, **12**, 7942–7947.
36 E. Garnett and P. Yang, *Nano Lett.*, 2010, **10**, 1082–1087.
37 L. Tsakalakos, J. Balch, J. Fronheiser, M.-Y. Shih, S. F. LeBoeuf, M. Pietrzykowski, P. J. Codella, B. A. Korevaar, O. V. Sulima, J. Rand, A. Davuluru and U. Rapol, *J. Nanophotonics*, 2007, **1**, 013552.
38 Z. Chen, T. F. Jaramillo, T. G. Deutsch, A. Kleiman-Shwarsctein, A. J. Forman, N. Gaillard, R. Garland, K. Takanabe, C. Heske, M. Sunkara, E. W. McFarland, K. Domen, E. L. Miller, J. A. Turner and H. N. Dinh, *J. Mater. Res.*, 2010, **25**, 3–16.
39 L. R. F. Allen and J. Bard, *Electrochemical Methods: Fundamentals and Applications*, John Wiley & Sons, Inc., 2001, 864.
40 B. E. Conway and G. Jerkiewicz, *Electrochim. Acta*, 2000, **45**, 4075–4083.
41 Y. Fujimoto and S. Saito, *J. Appl. Phys.*, 2014, **115**, 153701.
42 A. W. Bott, *Curr. Sep.*, 1998, **17**, 87–91.
43 K. Gelderman, L. Lee and S. W. Donne, *J. Chem. Educ.*, 2007, **84**, 685.
44 N. S. Lewis, *J. Electrochem. Soc.*, 1984, **131**, 2496–2503.
45 R. E. Hummel, *Electronic Properties of Materials*, Springer, 4th edn, 2011.
46 D. Merki, H. Vrubel, L. Rovelli, S. Fierro and X. Hu, *Chem. Sci.*, 2012, **3**, 2515–2525.
47 T. Lopes, L. Andrade, H. A. Ribeiro and A. Mendes, *Int. J. Hydrogen Energy*, 2010, **35**, 11601–11608.
48 J. Moon, J. An, U. Sim, S.-P. Cho, J. H. Kang, C. Chung, J.-H. Seo, J. Lee, K. T. Nam and B. H. Hong, *Adv. Mater.*, 2014, **26**, 3501–3505.

 This journal is © The Royal Society of Chemistry 2015